Wideband Synthetic Aperture Sonar Back Projection with Maximization of Wave Number Domain Support

Stig Asle Vaksvik Synnes, *Member, IEEE*, Alan Joseph Hunter, *Member, IEEE*, Roy Edgar Hansen, *Member, IEEE*, Torstein Olsmo Sæbø, *Senior Member, IEEE*, Hayden John Callow, *Member, IEEE*, Robbert van Vossen, Andreas Austeng, *Member, IEEE*

***Abstract*—Wideband and widebeam synthetic aperture sonar (SAS) can provide information on the frequency- and aspect-dependent scattering in a scene. We suggest an approach to predict the quality of the sensor data over the available frequencies and aspect angles. We relate the typical spatial domain quality metrics to their wavenumber domain counterpart, and use these to map the data quality in the wavenumber domain. Because SAS arrays often are under-sampled along-track, we pay particular attention to data degradation from aliasing. We use the proposed approach to examine how three SAS image formation algorithms based on time domain back projection access data of different quality from wideband SAS systems. We illustrate the results with predictions for a generic SAS design and demonstrate the findings on two experimental systems. We observe that the maximum support of high-quality data is achieved through back projection on to a high resolution grid followed by wavenumber domain filtering.**

***Index Terms*—Synthetic aperture sonar, back projection algorithms, wideband sonar, grating lobes, along-track ambiguity.**

I. Introduction

SYNTHETIC aperture sonar (SAS) has become an established technique for high resolution imaging of the seafloor [1], [2]. Wideband SAS can provide information on the frequency dependence of the acoustic bottom scattering, and at lower frequencies (LF) also of sub-bottom scattering. In addition, widebeam systems increase the probability of echo signals in directions with strong specular scattering [3]. Applications of LF wideband SAS include naval mine hunting and underwater unexploded ordnance (UXO) remediation with potential of improved detection and classification of both proud and buried targets, together with estimation of the probability of target burial [4], [5], [6], [7], [8]. Seabed mapping and characterization [9] and underwater archeology [10] may also take advantage of LF and wideband SAS. In this paper we let wideband denote systems with fractional bandwidth $B/f_c \gtrsim 1$, where B represents bandwidth and f_c the center frequency. The upper limit is a full bandwidth system of $B/f_c = 2$. Typical wideband SAS systems are also LF and include the SAMI (5-10 kHz) [11], BOSS (5-23 kHz) [3], MUD (1-4 kHz, 4-9 kHz, 11-26 kHz) [12] and HISAS with LF prototype extension (12-38 kHz concurrently with 60-85 kHz) [13]. In these systems the bandwidth at transmission is obtained using one to three transmitters, while at reception each element of the receiver array(s) cover the the entire frequency band.

SAS images map the scattering strength over the scene, and this is strongly influenced by its geometry. Wideband and widebeam systems also provide information on the frequency- and aspect-dependence of the scattering. In order to provide the best starting point for extracting the frequency- and aspect-dependence of scattering, we suggest building a SAS image with the maximum support of high-quality data. We consider different methods for preparing such a SAS image. We suggest that for the derivation of frequency- and aspect-dependence of the scattering, the SAS processing algorithms should be rated based on how they address data of different quality in the wavenumber domain, rather than on a spatial domain image quality that assumes frequency- and aspect-independent scattering. We develop wavenumber domain counterparts of the common spatial domain SAS image quality metrics. We apply these metrics on alternative wideband SAS imaging approaches and a typical SAS design, and on experimental data from two wideband LF SAS systems.

SAS image formation algorithms operate either in the time domain (TD) [14, chapter 4.1], [15, chapter 4.7] or in the wavenumber domain (WD) [15, chapter 4.5], [16, part II], [17, chapter 3]. In general the wavenumber domain algorithms are more efficient with respect to computational cost, but can be applied only for trajectories that closely align with one of the coordinate axes of a separable coordinate system. Linear track wavenumber domain imaging is most common, but also circular tracks have been accommodated [18]. The wavenumber domain algorithms can be adapted to handle small deviations to the ideal track, but at the cost of increased complexity and processing speed [19]. Time domain algorithms produce the

S. A. V. Synnes is with the Norwegian Defence Research Establishment (FFI), PO Box 25, N-2027 Kjeller, Norway, and is pursuing a Ph.D. at the University of Oslo (UiO), Department of Informatics, P.O. Box 1080 Blindern, N-0316 Oslo, Norway. Contact author e-mail: Stig-Asle.Synnes@ffi.no.

A. J. Hunter is with the University of Bath, Claverton Down Road, Bath BA2 7AY, United Kingdom.

R. E. Hansen is with the Norwegian Defence Research Establishment, and is also an adjunct associate professor with the University of Oslo, Department of Informatics.

T. O. Sæbø is with the Norwegian Defence Research Establishment.

H. J. Callow is with Kongsberg Maritime, Strandpromenaden 50, N-3183 Horten, Norway

R. van Vossen is with the Netherlands Organisation for Applied Scientific Research (TNO), Oude Waalsdorperweg 63, 2597 AK Den Haag, The Netherlands.

A. Austeng is with the University of Oslo, Department of Informatics.

Manuscript received May 6, 2015.

DOI til publisert versjon / DOI to published version: 10.1109/JOE.2016.2614717

best image quality for non-ideal trajectories, but are in general slower [20].

In this study we evaluate the performance of different SAS imaging approaches that starts with time domain back projection (BP). The beamwidth of wideband systems can change significantly with frequency, and processing the maximum valid beamwidth for all frequencies has the potential of providing the maximum information on the scene. However, standard BP image formation does not support processing frequency-dependent beamwidths. For wideband systems, splitting the signal into multiple bands and processing each band separately has been suggested to mitigate the negative effects of this limitation [21], [22]. However, new artifacts are introduced from merging sub-band images, as a result of the irregular shape of the combined wavenumber domain coverage. In Section III-C we investigate a third algorithm that takes full use of the available SAS information from wideband systems. This algorithm is based on time domain back projection followed by wavenumber domain filtering. We evaluate the extra computational load related to this hybrid time- and wavenumber domain algorithm.

Our main contribution is a new method for evaluating imaging algorithms, in which we address how they use the information on the scene provided by a wideband SAS system. Primary quality metrics for synthetic aperture imagery are resolution (mainlobe -3 dB width), peak sidelobe ratio, multiplicative noise ratio (from multipaths, sidelobes and grating lobes), additive noise level and geometric distortion [23, chapter 8.1], [24, chapter 6.2]. The relative importance of the image quality metrics strongly depends on the application, with its priority of resolution versus suppression of sidelobes and grating lobes [24, chapter 6.5].

We map the data quality in the wavenumber domain expressed through signal to ambient noise ratio (SNR) and signal to grating lobe ratio (SGR), and keep in mind that resolution is directly related to the wavenumber domain coverage. For each of the three imaging algorithms; back projection (BP), multiband back projection (MBP) and wideband back projection (WBP), we map their inherent windowing functions in the wavenumber domain. This allows us to investigate how the different imaging algorithms access data of different quality at different wavenumbers.

We show that the WBP method provides the best wavenumber domain data support, and thus also the best foundation for establishing any frequency- and aspect dependencies of the scattering strength. We do not attempt to address the quality of the corresponding full-band spatial domain imagery, but expect that the difference between the imaging algorithms will be less prominent as a result of reduced wavenumber domain coverage from the windowing functions used to suppress sidelobes, and from of any frequency- and aspect-dependence of the scattering. The validity of our approach for evaluating data quality is supported by real data measurements from a HISAS system with LF prototype extension on the HUGIN HUS autonomous underwater vehicle (AUV) of the Norwegian Defence Research Establishment (FFI) and from the MUD LF SAS prototype of the Netherlands Organisation for Applied Scientific Research (TNO).

In Section II we give a brief introduction to SAS image formation, address some of the challenges of wideband LF SAS image formation, and give an interpretation of SAS imaging in the wavenumber domain. In Section III we present the three algorithms for image formation in detail. We develop our approach for comparing the performance of different imaging algorithms in Section IV, with focus on the wavenumber domain data quality. Next we present our wavenumber counterpart to the spatial domain quality metrics in Section V. This is also where we compare the performance of the imaging algorithms through an investigation of coverage, SNR and SGR over the wavenumber domain. In Section VI we illustrate our findings on data from the two experimental LF SAS systems. Finally we conclude in Section VII.

II. SAS Imaging

SAS images represent information on the backscattering over a scene. In SAS image formation, data from multiple pings are combined coherently in order to synthesize an aperture that is significantly longer than the physical aperture. SAS thus provides increased resolution. Moreover, it provides resolution that is independent of range and frequency when using a fixed-size transducer for all frequencies [1]. Using the same elements over wide frequency spans is the common choice for many SAS-systems [3], [11], [12], [13].

A. Time Domain Back Projection

SAS image formation by time domain back projection (BP) is also known as delay-and-sum (DAS) beamforming. In this algorithm the received signal is back projected for each ping, from the receiver via each pixel in the scene and into the transmitter [14, chapter 4.1], [15, chapter 4.7]. This can be summarized as follows: Let i represent ping number, $\boldsymbol{u}_i$ the position along the platform trajectory at ping i and $\boldsymbol{x}$ represent the point to be probed (imaged). Let $\sigma(t)$ represent the received signal for the round-trip period $t(\boldsymbol{x}, \boldsymbol{u}_i)$; from the along-track position $\boldsymbol{u}_i$, to the pixel at position $\boldsymbol{x}$ and back, c.f. Fig. 1. We form the matched-filtered signal, $s_i(t, \boldsymbol{u}_i)$, by cross-correlating the received signal $\sigma(t)$ with the transmitted signal $p(t)$:

$$s_i(t, \boldsymbol{u}_i) = \sigma_i(t, \boldsymbol{u}_i) * p^*(-t). \tag{1}$$

The scattering coefficient can now be estimated using the expression

$$h(\boldsymbol{x}) = \frac{1}{\beta} \sum_{i \in i_\beta} \mathrm{w}(\theta(\boldsymbol{x}, \boldsymbol{u}_i)) s_i(t(\boldsymbol{x}, \boldsymbol{u}_i), \boldsymbol{u}_i) \Delta\theta(\boldsymbol{x}, \boldsymbol{u}_i), \tag{2}$$

where $\mathrm{w}(\theta)$ is an optional weighting function, and $\Delta\theta(\boldsymbol{x}, \boldsymbol{u}_i)$ is the angular span represented by ping i,

$$\Delta\theta(\boldsymbol{x}, \boldsymbol{u}_i) = \theta(\boldsymbol{x}, (\boldsymbol{u}_i + \boldsymbol{u}_{i+1})/2) - \theta(\boldsymbol{x}, (\boldsymbol{u}_i + \boldsymbol{u}_{i-1})/2). \tag{3}$$

Here $\theta(\boldsymbol{x}, \boldsymbol{u}_i)$ is the look angle, defined as the angle between the line of sight and the y-coordinate of the image. The summation of (2) is over all pings within the processing beamwidth β, i.e. $i_\beta = \{i | \theta(\boldsymbol{x}, \boldsymbol{u}_i) \in \langle -\beta/2, \beta/2 \rangle\}$, and the leading factor $1/\beta$ is a normalization on the processed beamwidth.

DOI til publisert versjon / DOI to published version: 10.1109/JOE.2016.2614717

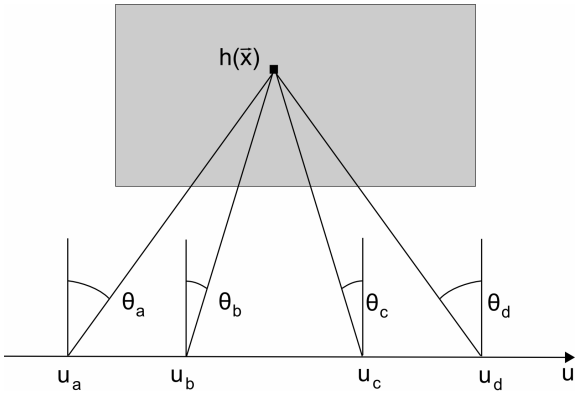

Fig. 1: Imaging geometry for transducer elements of the same size d on two frequency bands: The aperture from u_b to u_c is required to obtain resolution $d/2$ at the upper frequency band with -3 dB beamwidth of $\theta_b - \theta_c$, while the aperture u_a to u_d is required to obtain the same resolution at the lower frequency with -3 dB beamwidth of $\theta_a - \theta_d$. The corresponding image wavenumber domain coverages are shown in Fig. 2.

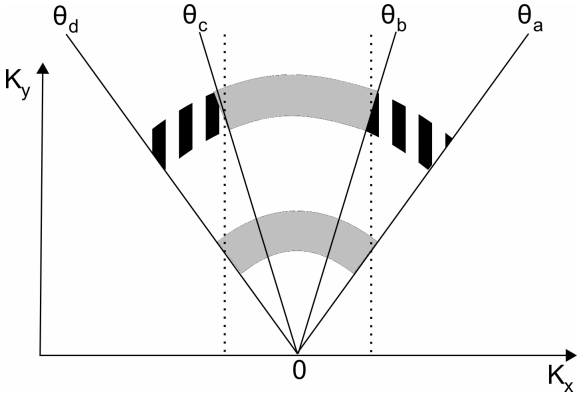

Fig. 2: Coverage in the image wavenumber domain for the upper and lower frequency bands of the imaging geometry in Fig. 1. The dotted lines indicate the -3 dB beamwidth for any frequency. The figure illustrates that when recording data within the -3 dB beamwidth at the low frequency (θ_a to θ_d), we record data within the -3 dB beamwidth at the high frequency (θ_b to θ_c), but also record undesired wavenumbers outside this region as indicated by the black striped areas. Alternatively the data can be processed from θ_b to θ_c, but then valid wavenumbers would be missing for the low frequency.

The received signal must be sampled in accordance with the Nyquist criterion, both temporally and spatially, in order to eliminate aliasing (ambiguities) [14, chapter 3.2]. Artifacts caused by spatial aliasing are commonly referred to as grating lobes.

As mentioned in Section I, a limitation of time domain back projection is that the processing beamwidth is independent of frequency and the same limitation also applies to the weighting function $\mathrm{w}(\theta)$.

The SAS image formation described in (2) does not account for geometric spreading and absorption, nor for the element beampattern. However, it is straightforward to account for the spreading loss in the time domain matched filtering and the element beampattern in the wavenumber domain. The absorption loss is both frequency- and range dependent, but can also be accounted for in a matched filter.

B. Challenges of Wideband SAS

Challenges of SAS imaging include requirements on navigation accuracy, sound speed accuracy and bathymetric accuracy, together with multiplicative noise due to multipath [25].

In this paper we address the wideband-specific challenge of processing a frequency dependent beamwidth. This challenge must be met in order to include data for processing based on the data quality. The relevance of the problem is illustrated in Fig. 1, showing the synthetic apertures (and span of azimuth-angles) at two frequencies for a wideband SAS system. In order to fully exploit the sensor data, frequency-dependent processing beamwidth is required. This becomes increasingly more important for systems with higher fractional bandwidth.

C. Image Wavenumber Spectrum

The image wavenumber spectrum is important for wideband data analysis, as it can be interpreted as a map of the response of scene and processing as a function of frequency and look angle. Furthermore, the wavenumber coverage has a direct relation to the point-spread function, and we will later investigate how the various imaging algorithms can be distinguished from one another by addressing the shape of their image wavenumber domain coverage.

We let the image wavenumber spectrum $H(\boldsymbol{K})$ be the 2D Fourier transform of the complex SAS image $h(\boldsymbol{x})$, denoting the image wavenumber vector $\boldsymbol{K}$, following [15, chapter 4], [26, chapter 4.3], [18]. The image wavenumber vector, also known as the Bragg wavenumber vector or the scattering wavenumber vector, expresses the difference between the reflected and incident wavenumber vectors, $\boldsymbol{k}_{re}$ and $\boldsymbol{k}_{in}$, of the target scattering for a general bi-static configuration [27, Section 16-2]:

$$[K_x, K_y] = \boldsymbol{K} = \boldsymbol{k}_{re} - \boldsymbol{k}_{in}. \tag{4}$$

For small baseline (distance between transmitter and receiver) we can make the approximations:

$$|\boldsymbol{K}| \approx 2k, \text{ where } k = \frac{2\pi f}{c} \tag{5}$$

$$\angle \boldsymbol{K} \approx \theta \tag{6}$$

which correspond to a monostatic transmitter/receiver configuration. Here k is the propagating wavenumber at frequency f for phase velocity c, while θ is the aspect angle at which each pixel is observed. In order to give an alias-free representation of the image wavenumber spectrum with discrete sampling, the image grid must meet the Nyquist criterion over the span of the processed bandwidth and beamwidth.

In Fig. 2 we illustrate how the image wavenumber spectrum is populated, given the geometry of Fig. 1. The processed pings are being distributed over an arc length proportional to K, such that the sample density in the K_x, K_y-plane is proportional to $1/K$.

DOI til publisert versjon / DOI to published version: 10.1109/JOE.2016.2614717

The relation between the spatial image and the image wavenumber spectrum is illustrated on real data in Fig. 3 and Fig. 4, and the image has been formed using the wideband back projection algorithm of Section III-C. The SAS data were recorded by HISAS with a LF prototype extension. Here the

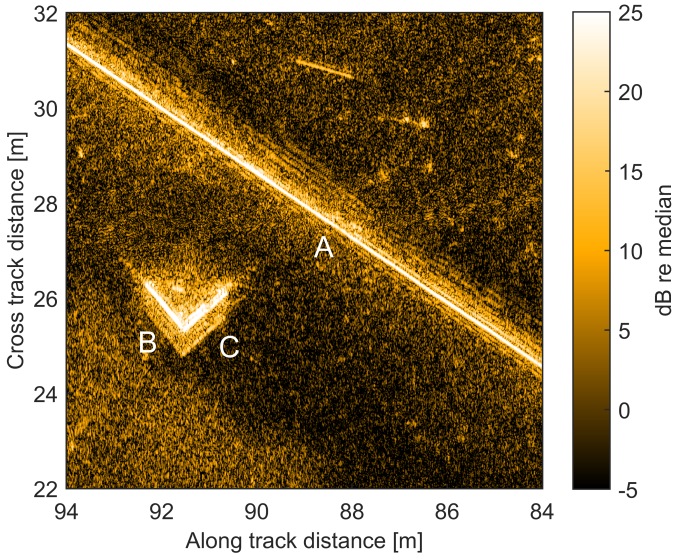

Fig. 3: Spatial domain SAS image at 12-38 kHz processed over the -3 dB bandwidth indicated in Fig. 4. The image shows a 1.2 m x 1.2 m concrete block next to a 0.9 m diameter pipeline. The collected wavenumber domain spectrum is shown in Fig. 4. The data were recorded by HISAS with a LF prototype extension on FFI's HUGIN autonomous underwater vehicle during ARISE'12.

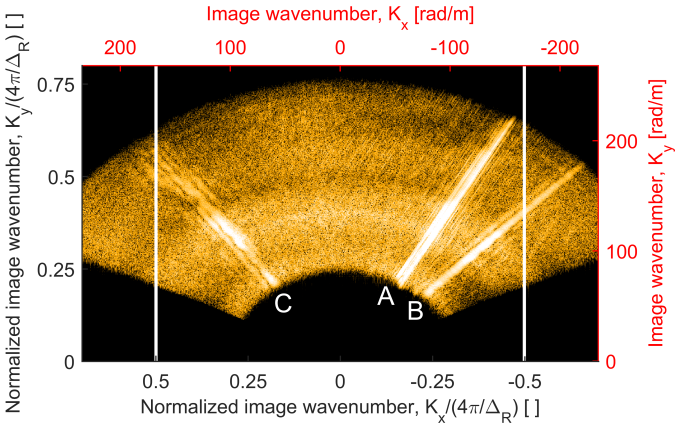

Fig. 4: Image wavenumber domain spectrum for the aperture used in the SAS image of Fig. 3. The vertical white lines roughly indicate the -3 dB bandwidth. We can relate the strong lines of the spectrum to specular reflections off the pipe (A), the lefthand side of the cube (B) and the righthand side of the cube (C).

wavenumber spectrum contains all the data collected on the scene, and the image was formed by processing the along-track wavenumbers K_x over the span indicated by the vertical lines, and compensating for the sample density of $1/K$. We recognize the specular reflection off the pipe (A), the lefthand side of the cube (B) and the righthand side of the cube (C) in Fig. 3 as strong lines in the wavenumber spectrum, correspondingly labeled (A), (B) and (C) in Fig. 4. The image was formed in the ground range coordinate system $[x, y]$ and not in the slant range system $[x, \sqrt{y^2+z^2}]$.

In order to support transition of the results to other systems, we have normalized the image wavenumber coordinates by $4\pi/\Delta_R$, where Δ_R is the receiver array element spacing. For dense receiver arrays with rectangular elements of size $d_R = \Delta_R$, this normalization is numerically identical to normalizing to half the full mainlobe width (i.e. half the null-to-null bandwidth). In addition to the normalized values (in black), we also give the numerical values for the system used (in red), as in Fig. 4.

III. Wideband Imaging Methods

In this section we present three algorithms for wideband SAS image formation.

A. Back Projection (BP)

Standard BP image formation was outlined in Section II-A. The algorithm is illustrated schematically in Fig. 5a, and follows the formulation given in (2). We observe that the windowing is independent of frequency, as the weights $\mathrm{w}(\theta)$ only change with look angle θ to the pixels from each element in the synthetic aperture. For comparison with the other algorithms, we adopt the along-track wavenumber coverage at the center of the frequency band as the effective coverage, in a compromise between missed low frequency data and added high frequency data, c.f. Fig. 2, and obtain $\Delta K_{x_{eff}} \approx 2K(f_c)\sin(\beta/2)$.

B. Multiband Back Projection (MBP)

Multiband back projection is also known as the subband method or spectral decomposition [21], [22]. The idea of the multiband algorithm is to split the signal into multiple narrower bands in order to approach a more rectangular wavenumber coverage. The multiband back projection method can be expressed through (7), where N is the number of subbands, and $s_i(n, t, \boldsymbol{u}_i)$ and $\beta(n)$ are respectively the bandpass filtered data and the processing beamwidth for subband n.

$$h(\boldsymbol{x}) = \sum_{n=1}^{N} \frac{1}{\beta(n)} \sum_{i \in i_{\beta(n)}} \mathrm{w}(\theta(\boldsymbol{x}, \boldsymbol{u}_i)) s_i(n, t(\boldsymbol{x}, \boldsymbol{u}_i), \boldsymbol{u}_i) \Delta\theta(\boldsymbol{x}, \boldsymbol{u}_i). \tag{7}$$

In Fig. 5b we illustrate the processing flow of the multiband algorithm. After splitting the signal into multiple subbands, the standard BP algorithm is applied on each individual band, before the processed subband images are summed coherently to produce the MBP image. The multiband approach can introduce artifacts from merging the discrete bands, as a result of the irregular shape of their combined wavenumber domain coverage.

DOI til publisert versjon / DOI to published version: 10.1109/JOE.2016.2614717

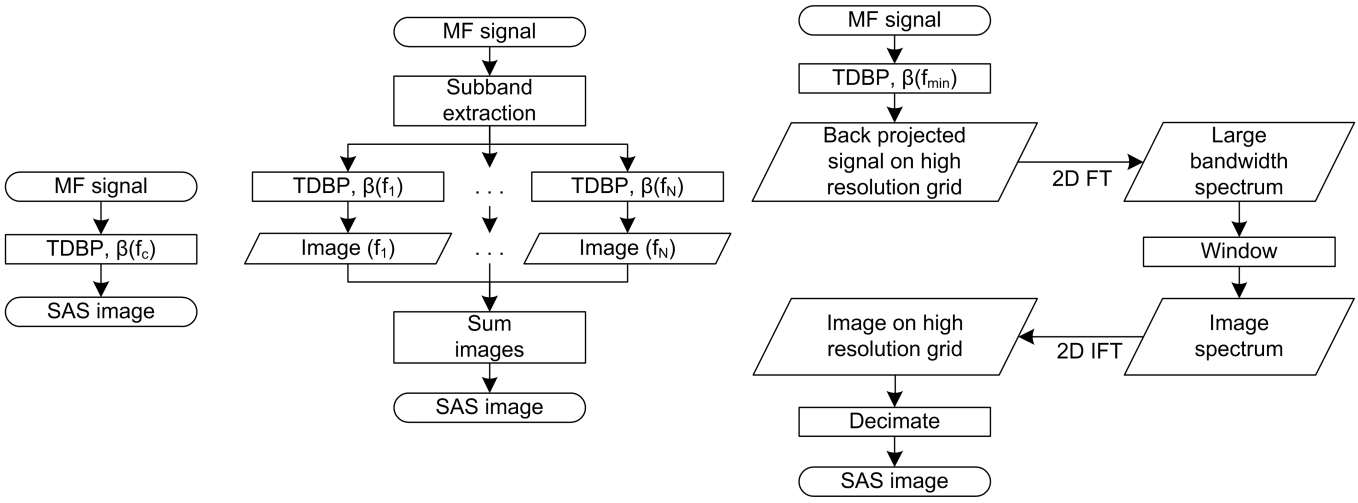

(a) Back Projection (b) Multiband Back Projection (c) Wideband Back Projection

Fig. 5: Image formation processing flow for a) the standard Back Projection (BP) algorithm, using the same processing beamwidth β for the entire signal bandwidth, b) the Multiband Back Projection (MBP) algorithm, dividing the signal bandwidth into multiple subbands and using the standard back projection algorithm on each subband and c) the Wideband Back Projection (WBP) algorithm, performing frequency-dependent windowing in the wavenumber domain.

C. Wideband Back Projection (WBP)

Wideband back projection supports any wavenumber domain coverage, including rectangular. The approach is based on time domain back projection followed by wavenumber domain filtering [13]. It is thus a hybrid time/wavenumber domain approach.

We illustrate the main steps of the wideband algorithm in Fig. 5c. First, the signal is back projected using the maximum processing beamwidth imposed by the lowest frequency. We use a high resolution grid that meets the Nyquist criterion over the processed bandwidth and beamwidth, thus supporting a discrete Fourier transform into the image wavenumber domain. Here we apply the desired processing bandwidth by means of a windowing function. Then, returning to the spatial image domain (for numerical reasons only) we decimate the data in order to obtain the requested spatial grid of the final SAS image.

The approach can be described in a spatial (or time) domain representation through (8) for comparison with the other algorithms. We let $(*_{x,y})$ denote a 2D convolution along both the x- and y-axis. The back projected maximum beamwidth wideband signal is expressed in (10), and the processing beamwidth is defined through the wavenumber domain windowing function W of (9).

$$h(\boldsymbol{x}) = \mathrm{w}(\boldsymbol{x}) *_{x,y} h_0(\boldsymbol{x}), \tag{8}$$

where

$$\mathrm{w}(\boldsymbol{x}) = IFT_{2D}\{W(\boldsymbol{K})\} \tag{9}$$

and

$$h_0(\boldsymbol{x}) = \frac{1}{\beta(f_{min})} \sum_{i \in i_{\beta(f_{min})}} s_i(t(\boldsymbol{x}, \boldsymbol{u}_i)) \Delta\theta(\boldsymbol{x}, \boldsymbol{u}_i). \tag{10}$$

The sampling requirement of the WBP algorithm follows from its maximum wavenumber coverage: The output image of the WBP algorithm ideally has the same along-track image wavenumber coverage, $\Delta K_{x_{image}}$, at all frequencies, representing a frequency-dependent processed beamwidth. While the largest beamwidth is required for populating the lowest frequency data only, all frequencies are populated with the back projection processing. As a result, the highest frequency data will span an along-track image wavenumber coverage of $\Delta K_{x_{Nyquist}} = \Delta K_{x_{image}} \frac{f_{max}}{f_{min}}$, and in order to avoid any aliasing, the sampling grid must support $\Delta K_{x_{Nyquist}}$. However, because wavenumbers outside $\Delta K_{x_{image}}$ is excluded from the output image, aliasing in that region does not affect the output image. As a result, the maximum along-track image wavenumber coverage required for the WBP algorithm is $\Delta K_{x_{WBP}} = \Delta K_{x_{image}} \frac{f_{max}+f_{min}}{2f_{min}}$. The corresponding cross-track image wavenumber coverage required for the WBP algorithm is $\Delta K_{y_{WBP}} = K(f_{max}) - K(f_{min})\cos(\beta(f_{min})/2) \lesssim K(f_{max})$. The related pixel spacing follows from the Fourier relation $[d_x, d_y] = [2\pi/\Delta K_x, 2\pi/\Delta K_y]$.

IV. Performance Evaluation

We argue that the relative performance of the different algorithms for image formation cannot be established solely by evaluating the image quality of large bandwidth images. In particular, wideband and widebeam data fully contribute to improved resolution only where the scattering can be modeled by a point target at a fixed position, independent of frequency and aspect angle [28]. This criterion is typically not met for wideband widebeam systems, with frequency-dependent scattering and a higher potential of aspect-dependent occlusion. The full bandwidth and beamwidth is nontheless important for the analysis of frequency- and aspect-dependent scattering [5], [6]. Furthermore, any image will inevitably incorporate application-dependent design choices [24, section 6.5] and of course also the scene contents. We suggest an approach for isolating the performance of the imaging algorithms from

DOI til publisert versjon / DOI to published version: 10.1109/JOE.2016.2614717

the impact of system and scene, thus providing the means to compare and evaluate the performance of the algorithms.

A. Spatial Domain Evaluation

As cited in Section I, the synthetic aperture literature typically uses resolution (mainlobe -3 dB width), peak sidelobe ratio, multiplicative noise ratio (from multipaths, sidelobes and grating lobes), additive noise level and geometric distortion as primary image quality metrics. The relative importance of the image quality metrics strongly depends on the application. In particular, a compromise must be made between resolution and suppression of sidelobes and grating lobes.

We assume that additive noise, multipath and defocus/geometric distortion (from inaccurate assessment of navigation, medium and/or bathymetry) should have roughly the same impact on the investigated SAS imaging algorithms. However, the inherent windowing function of the imaging algorithms can have different impacts on resolution, peak sidelobe ratio and multiplicative noise ratio (from integrated sidelobe ratio and integrated grating lobe ratio). The latter metrics with potential of discriminating between the processing algorithms can all be derived from the point spread function (PSF), which depicts how a system reproduces a single point scatterer [24, chapter 6.2].

Unfortunately, neither the point spread function, nor all of the image quality metrics can easily be computed from an image of opportunity. In SAR, evaluating the performance of a specific system typically involves imaging a strong point scatterer in order to obtain an estimate of the point spread function [23, chapter 8.7]. An indication of the performance for a specific system can also be obtained by simulating a point scatterer as seen through the system [24, chapter 6.5]. The performance of a specific system is determined by the system design and the processing choices, both ideally optimized for the systems' intended application.

B. Wavenumber Domain Evaluation

We choose to evaluate and compare the different algorithms for image formation in the wavenumber domain, with focus on the metrics that can be derived from the point spread functions. The wavenumber domain is chosen because the differences between the three algorithms are more naturally observed in this domain. We assess the data quality as a function of wavenumber, and rate the different algorithms by how well they target the data.

We divide the system point spread function into two wavenumber domain components, the *sensed spectrum* and the *windowing function* as illustrated in Fig. 6. The sensed spectrum represents the scattering coefficients of the scene in the wavenumber domain, filtered by the system response. The windowing function describes the $\boldsymbol{K}$-dependent weighting of the imaging algorithm, and determines the trade-off between resolution and contribution from background noise, sidelobes and grating lobes.

For simplicity, we assume that both the spectrum and the amplitude distribution of the real world scattering coefficients are homogeneous and thus can be ignored in the performance assessment. The remaining components are then the sensor response and the windowing function, where the sensor response reflects the design choices, and the windowing function reflects the processing choices. Both should ideally be optimized for the application based on a set of performance metrics.

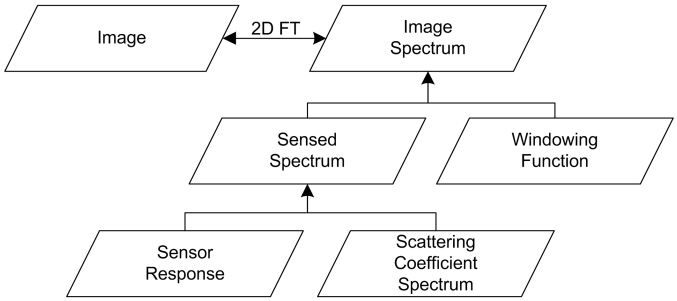

Fig. 6: Decomposition of the image data in the wavenumber domain. The point spread function is addressed when the imaged scene only contains a single point scatterer.

We choose to assess how SGR, SNR, resolution and sidelobe level depends on typical design choices and the image formation algorithms. The established way of evaluating the effect of different windowing functions is to start with measured or simulated data from a point scatterer, and for each candidate windowing function generate spatial domain images and estimate their quality metrics. In our complementary approach we emphasise how different factors affect the data quality by mapping the quality metrics SGR and SNR as function of image wavenumber $\boldsymbol{K}$. Based on these maps we analyse how each algorithm accesses data of different quality.

V. Wavenumber Domain Performance Metrics

We develop a set of wavenumber domain performance metrics and consider how the imaging algorithms access data of different quality over the wavenumber domain:

- The shape and distribution of the weighting function $W(\boldsymbol{K})$ inherent to each imaging algorithms is mapped over the sensed spectrum as a function of $\boldsymbol{K}$.
- The algorithm-independent properties of the weighting function $W(\boldsymbol{K})$ related to resolution, sidelobe level and homogeneity are treated separately.
- The data quality is expressed through the SNR over the sensed spectrum as a function of $\boldsymbol{K}$.
- The data quality is expressed through the SGR over the sensed spectrum as a function of $\boldsymbol{K}$.

A. Algorithm-Dependent Window Shape

The main differences between the output of the three evaluated algorithms for image formation are their inherent wavenumber domain window shapes and the coordinate along which the weights are applied. We illustrate the window shapes in Fig. 7 for each of the algorithms. The BP algorithm only supports weighting on the look angle θ. The weighting of the MBP algorithm is related to that of BP, but with weights determined independently for each frequency band. The WBP algorithm supports any windowing function, but we

DOI til publisert versjon / DOI to published version: 10.1109/JOE.2016.2614717

limit this study to functions on the along-track wavenumber, K_x. Processing a window covering half the zero-crossing beamwidth at all frequencies corresponds to a frequency-dependent beamwidth $\beta_{00/2}(f) = 2\sin^{-1}\left(\Delta K_{x,00/2}/2K\right) = 2\sin^{-1}\left(\lambda(f)/2d_R\right) \approx \lambda(f)/d_R$, where $\lambda = c/f$, and the approximation applies for $\lambda < d_R$.

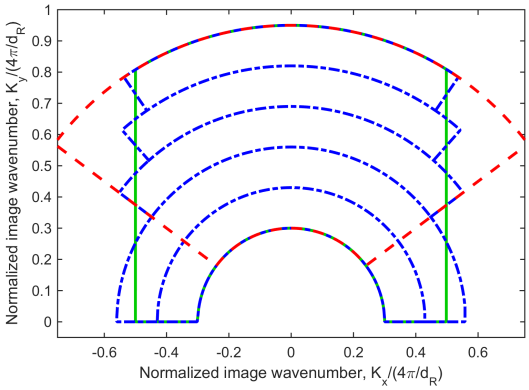

Fig. 7: Illustration of the image wavenumber coverage of three algorithms with cutoff at half the receiver element zero-crossing beamwidth (roughly the -3 dB beamwidth), evaluated at the center frequency of each band for a system with fractional bandwidth $B/f_c = 1$: BP algorithm (red), MBP algorithm (blue) and WBP algorithm (green).

B. Algorithm-Independent Weighting Function

Through the choice of weighting function, resolution and wavenumber coverage is traded for reduced grating lobe level and reduced sidelobe level [23, chapter 8.3]. In order to retain as much as possible of the information on the scene and also obtain the maximum resolution, the window should be as wide as possible while sustaining the required signal to noise level. In order to constrain the (integrated) sidelobe level, the window should have a smooth roundoff. In order to approach uniform sensitivity, the center of the window should be as flat as possible. This gives a set of conflicting requirements, and a compromise must be made based on the application.

In order to obtain valid estimates of the backscattering strength for all look angles, beampattern compensation should be incorporated into the weighting function.

C. Signal to Ambient Noise Ratio

Ambient noise limits the data quality, and can be expressed in the image wavenumber domain by the signal to ambient noise ratio as a function of image wavenumber.

The signal intensity over the image wavenumber is proportional to the element beampattern as a function of frequency. SAS elements are typically used over a wide range of frequencies and can often be represented by rectangular transducers with length d. The one-way amplitude response, A, of a rectangular element of length d is in the $[k_x, k]$-domain given by

$$A(k_x, k) = \begin{cases} |d|\mathrm{sinc}\left(\frac{k_x}{2\pi/d}\right) & k \in [k_{min}, k_{max}] \\ 0 & \text{otherwise} \end{cases}, \quad (11)$$

where sinc denotes the normalized sinc-function, while k_{min} and k_{max} are the lower and upper wavenumbers in the bandwidth. The combined transmitter/receiver response is proportional to the signal to ambient noise ratio with white isotropic noise, illustrated in the upper panel of Fig. 8 for the case of equally sized transmitter and receiver elements, $d_T = d_R$. In

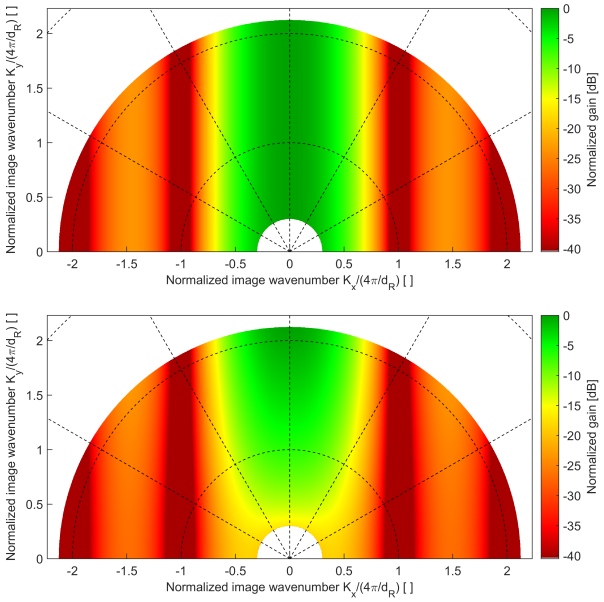

Fig. 8: Signal to ambient noise ratio assuming isotropic noise (upper panel) and assuming 1/f-amplitude noise (lower panel), both normalized to unity at broadside and for the maximum frequency. Equally sized rectangular transmitter and receiver elements, $d_T = d_R$, are assumed, and the illustrated image wavenumber support covers both LF and MF bands of the HISAS system.

practice, the ambient noise spectrum in the 1-50 kHz band is better approximated by a $1/f$ amplitude dependence [29], and the corresponding signal to ambient noise ratio is illustrated in the lower panel of Fig. 8. For a flat noise spectrum, the signal to ambient noise ratio is a function on K_x only, and the WBP algorithm would provide access to all data above a given quality. With $1/f$ noise, the signal to ambient noise ratio is not perfectly matched by the window function of neither the BP nor the WBP algorithm, but for large beamwidths the WBP algorithm provides a significantly better discrimination between high- and low quality data.

D. Signal to Grating Lobe Ratio

SAS arrays are often under-sampled along-track in a compromise between coverage rate, complexity, cost and data quality. Under-sampling of the aperture will give rise to *grating lobes* (azimuth ambiguities / aliasing of energy) and

DOI til publisert versjon / DOI to published version: 10.1109/JOE.2016.2614717

degrade the SAS image quality [24, chapter 6.5.1], [30], [31]. When using multi-element receiver arrays, the receiver element spacing Δ_R is normally equal to the receiver element size d_R. In accordance with the Shannon Nyquist sampling theorem, these multi-element SAS systems are well-sampled only when $d_R = \Delta_R < \lambda_{min}/2$.

The response of the SAS aperture (including grating lobes) is expressed by its aperture function, and can be represented by the combined transmitter/receiver element beampattern, convolved by the synthesized receiver array positions [30], [31]. The image wavenumber domain response of a sampling function with spacing Δ_R along x is a Dirac comb-function along K_x with periodicity $\Delta_{K_x} = 2\Delta_{k_x} = 4\pi/\Delta_R$. When imaging a pixel, the entire Dirac comb-function is shifted, and contributions to grating lobes occur when the peaks of the Dirac-comb fall inside the sidelobes of the beampattern. Thus, for an under-sampled SAS array, $\Delta_R > \lambda_{min}/2$, and for the common case of element size $d_R = \Delta_R$, there are no grating lobes when processing broadside data only. However, the impact of grating lobes increases with increasing processing beamwidth, as off-broadside data is included [30]. This process is illustrated in Fig. 9, where the response of the sampling function, illustrated for processing broadside data, is overlaid on the combined transmitter/receiver beampattern for a system with $d_T = d_R = \Delta_R$. When processing off-broadside data the grating lobes no longer align with the nulls of the beampattern, and their impact increases. The angle of observation related to processing a specific image wavenumber $\boldsymbol{K}$ follows from (6). The beampattern at $|K_x| > K$ corresponds to evanescent waves that decay very rapidly. These are therefore neglected in the following.

Grating lobes affect the wavenumber spectrum in the $[K_x, K]$ coordinate system by replicating the spectrum of the scene at periodicity $4\pi/\Delta_R$ along K_x. The related image wavenumber spectrum in $[K_x, K_y]$ is obtained by applying the Stolt transform [23, chapter 10.2.3]. For narrowbeam systems, $K_y \approx K$, and any grating lobes give object replica at a fixed spatial interval Δ_{x_G} along the x-axis for range r:

$$\Delta_{x_G} = r\lambda/\Delta_R. \tag{12}$$

A distortion of the targets are introduced as K_y diverts from K with increasing beamwidth. Regardless, for the case of wideband widebeam systems, a much stronger blurring is introduced from a large relative bandwidth. Both effects can be observed and inspected in the real data image wavenumber spectrum of Fig. 16, which is addressed in Section VI-B.

How the impact of grating lobes is perceived depends on the application of the image; in particular whether we are interested in speckle or in persistent scatterers. These two cases correspond to studying signals with, respectively, zero or full correlation over the covered frequency and angular span. The degradation experienced for each case depends on the degree of defocus of the grating lobes. We simplify our analysis by limiting it to wideband widebeam systems with at least a few persistent scatterers distributed over the scene, such that the grating lobes are strongly defocused. We study the SGR for a speckle scene in detail, before we briefly address some

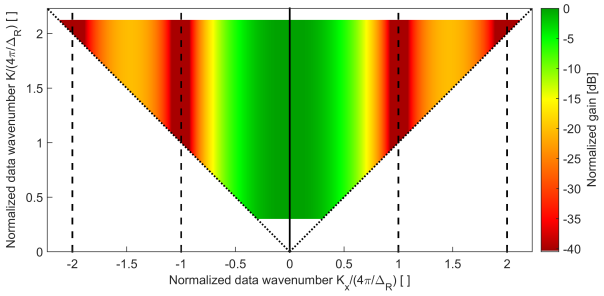

Fig. 9: Combined transmitter/receiver normalized gain along with the sampling function response corresponding to an infinitely long array with broadside steering. The image wavenumber spectrum will contain the sum of both the main-lobe value (solid line) and the grating lobe values (dashed lines). For off-broadside steering, both solid and dashed lines are shifted equally. The elements have been assumed rectangular with transmitter and receiver dimensions $d_R = d_T = \Delta_R$, where Δ_R is the element spacing. Non-propagating waves, outside the white lines are not shown. Note that the shown wavenumber coverage is in the $[K_x, K]$ coordinate system, and *not* in the $[K_x, K_y]$ coordinate system. This choice reflects the native coordinate system of the data recording, and thus the axis along which aliasing can originate. The illustrated wavenumber support covers both LF and MF bands of the HISAS system used in the examples.

modifications that apply with the introduction of persistent scatterers.

1) Speckle: For speckle the signal does not add up in phase over look angles and frequency span. The average spatial domain SGR corresponds to the integrated signal to integrated grating lobe ratio (ISIGR) in the wavenumber domain. This is given in [24, chapter 6.5.1] through its reciprocal, the along-track ambiguity to signal ratio (AASR), assuming narrowband and homogeneous scattering distribution. This expression is extended to include weighting over the processing beamwidth in [32, chapter 5.2.1]:

$$ISIGR(\Delta K_x, K_y) = \frac{\int\limits_{\Delta K_x} W(\boldsymbol{K}) S(\boldsymbol{K})\, dK_x}{\int\limits_{\Delta K_x} W(\boldsymbol{K}) G(\boldsymbol{K})\, dK_x}, \tag{13}$$

where

$$S(\boldsymbol{K}) = Z\left\{A^2(K_x, K)\right\} \tag{14}$$

and

$$G(\boldsymbol{K}) = Z\{\sum_{\substack{m=-\infty \\ m\neq 0}}^{\infty} A^2(K_x + m\frac{4\pi}{\Delta_R}, K)\} \tag{15}$$

are the signal energy and the grating lobe energy respectively, and $Z\{\cdot\}$ denotes the Stolt transform from $[K_x, K]$ to $[K_x, K_y] = \boldsymbol{K}$. Δ_{K_x} expresses the along-track processing bandwidth. The weighting $W(\boldsymbol{K})$ expresses the algorithm-dependent window shape of Section V-A for the chosen processing beamwidth or bandwidth and the weighting function of Section V-B applied within the window. The weighting

DOI til publisert versjon / DOI to published version: 10.1109/JOE.2016.2614717

can optionally include beampattern compensation through a scaling by $1/S(\boldsymbol{K})$.

Equation (13) gives an average result over the processed wavenumber domain spectrum, and thus gives a data or system quality metric. We introduce a new means for analyzing the data quality by mapping and evaluating the signal to grating lobe ratio as function of image wavenumber,

$$SGR(\boldsymbol{K}) = \frac{S(\boldsymbol{K})}{G(\boldsymbol{K})}. \tag{16}$$

The SGR thus provides the quality of the added data from changing the processing beamwidth or the window shape.

In Fig. 10 we present the predicted SGR for a typical SAS design of a dense linear receiver array and equally sized transmitter and receiver elements. We observe that we have both a well-sampled and an under-sampled region. The well-sampled region covers the wavenumbers where the along-track array fulfills the Shannon-Nyquist sampling theorem, or $|\boldsymbol{K}|/(4\pi/\Delta_R) < 0.5$. Because we assume that there is no signal arriving from the backside of the array ($K_y < 0$ in the figures), there is a larger region with no aliasing, covering wavenumber vectors fulfilling $(|\boldsymbol{K}| + |K_x|)/(4\pi/\Delta_R) < 1$. For the under-sampled region, we observe that the SGR is a function of K_x only. Taking full advantage of all well-sampled data, together with the under-sampled data up to a given quality, would require a tailored 2D-windowing function.

2) Persistent scatterers: The findings of the previous section address incoherent scatterers. For persistent scatterers the signals add up in phase over look angles and frequency span, and most targets of interest will be in phase over a span of look angles and frequencies. Assuming that the corresponding grating lobes are added out of phase, this will result in a significant increase of ISIGR versus that estimated for speckle, despite the wavenumber domain SGR being the same. As a consequence, targets might be observed in images also when zero or negative ISIGR is estimated for the speckle case [24, Section 6.5.1].

VI. Results and Discussion

We first present the predicted performance for a common but idealized SAS system design, and for two existing LF wideband SAS systems. For the existing systems we also include results on measured data for validation of the predicted performance.

Most SAS systems use a uniform linear array with along-track element size similar to the element spacing. These are typically under-sampled along-track for a portion of the frequency band, c.f. Section V-D. As a result, the impact of grating lobes is the main candidate for limiting the data quality. We therefore focus on mapping the SGR in the wavenumber domain, and perform the performance predictions for such a system. We also include performance predictions for simplified models of the HISAS with LF prototype extension, and from the MUD prototype SAS. We have also collected experimental data on these two SAS systems. These systems are shown in Fig. 14. Both systems are under-sampled for a portion of their

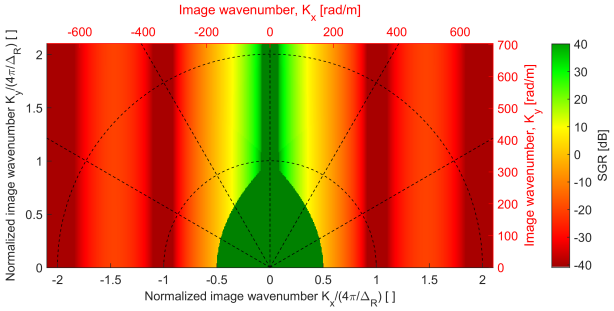

Fig. 10: Main lobe to grating lobe ratio for systems with $d_T = d_R = \Delta_R$.

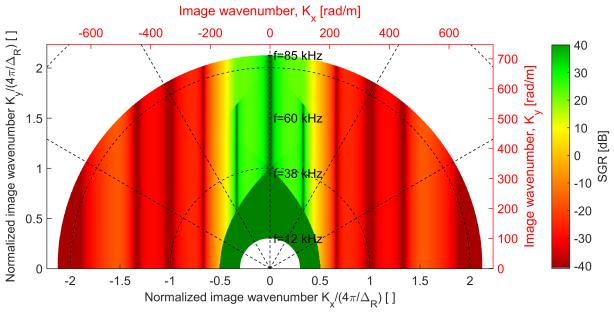

Fig. 11: Main lobe to grating lobe ratio corresponding to the HISAS with LF prototype extension, represented by $d_T 2/3 = d_R = \Delta_R = 3.75$ cm, and illustrated for the frequency interval 12-85 kHz, covering the LF (12-38 kHz) and MF (60-85 kHz) bands.

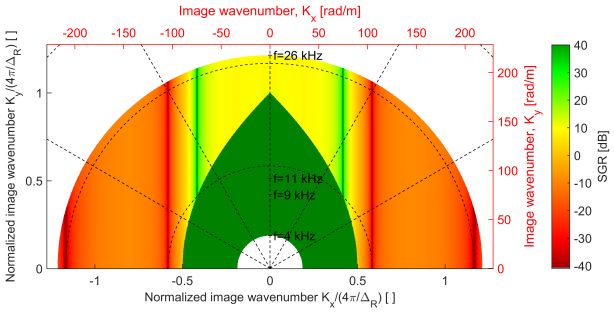

Fig. 12: Main lobe to grating lobe ratio corresponding to the MUD system in the horizontal configuration, represented by $d_T = 0.12$ m, $d_R \approx 0.03$ m, $\Delta_R = 0.07$ m, and illustrated for the frequency interval 4-26 kHz.

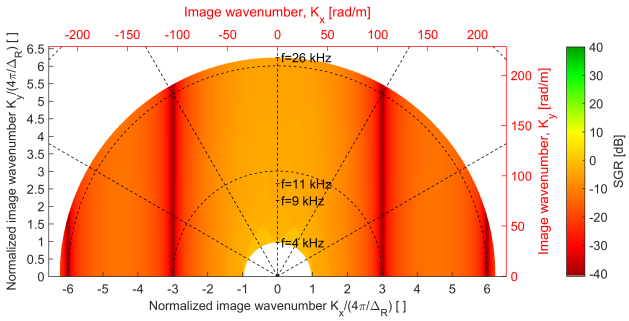

Fig. 13: Main lobe to grating lobe ratio corresponding to the MUD system in the vertical configuration, represented by $d_T = 0.12$ m, $d_R \approx 0.01$ m, $\Delta_R = 0.36$ m (effective multi-element receiver spacing), and illustrated for the frequency interval 4-26 kHz. The configuration provides a significantly lower grating lobe suppression than the design choice of the horizontal configuration. At the measurement site, multipath suppression showed to be of the utmost importance, and for this the vertical configuration was superior.

DOI til publisert versjon / DOI to published version: 10.1109/JOE.2016.2614717

frequency band, such that the data quality is limited by SGR off broadside also for the experimental systems.

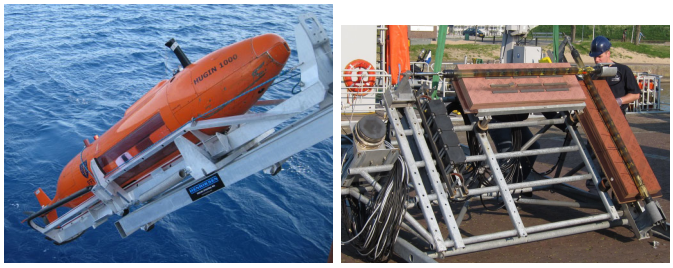

Fig. 14: Left: FFI's HUGIN HUS AUV carrying the HISAS system with prototype LF transmitter, during launch from CMRE's R/V Alliance. Right: TNO's MUD LF SAS prototype before operation from a diver support vessel of the Royal Netherlands Navy.

For the experimental data recordings, HISAS was operated from FFI's HUGIN HUS autonomous underwater vehicle, and the datasets were collected during the ARISE'12 (Autonomous Reactive Intelligence Sea Experiment) organized by the NATO Centre for Maritime Research and Experimentation (CMRE) [13]. The LF band on HISAS spanned 12-38 kHz and was operated concurrently with a MF band spanning 60-85 kHz. We present theoretical predictions for the full band case and experimental results from the LF band. The experimental data from TNO's MUD LF SAS prototype were collected during the MUD-2011 sea trial in Haringvliet, where it was operated from a diver support ship of the Royal Netherlands Navy [12]. The system has three transducers, covering the frequency bands 1-4 kHz, 4-9 kHz and 11-26 kHz. The MUD system was designed as an interferometric SAS, with two along-track arrays that meet the Shannon-Nyquist sampling criterion below 11 kHz. Because of severe multipath at low frequencies in the 10-15 m water depth of the trial, data was also recorded with one of its receiver arrays mounted vertically. This allowed for better multipath suppression through vertical beamforming [33]. With the along-track array reduced to only one effective element, the data from the MUD system in the vertical configuration was under-sampled above 4 kHz. We present theoretical predictions for both configurations using the full band, but experimental results for the vertical configuration with transmission in the 4-9 kHz band only.

A. Theoretical Results on Wavenumber Domain Data Quality

We present the performance prediction on SGR for a uniform linear array with along-track element size similar to the element spacing in Fig. 10, where we include frequencies that cover the transition from a well-sampled to an under-sampled system. In Fig. 11, Fig. 12 and Fig. 13 we present the predicted SGR for our experimental systems, modeled by their corresponding transmitter length d_T, receiver length d_R and receiver spacing Δ_R, available from the figure captions. Fig. 11 corresponds to the HISAS LF and MF bands, Fig. 12 to MUD operated in the horizontal configuration for the frequency span 1-26 kHz, and Fig. 13 to MUD operated in the vertical configuration for the same frequency band.

We observe that the SGR for the experimental systems is in line with the predictions for the generalized system design of Fig. 10. To access all under-sampled data above a given SGR, together with all well-sampled data, would require a tailored 2D-window. In the under-sampled region, the SGR is a function on K_x only.

B. Experimental Validation of Wavenumber Domain Performance Evaluation

In the presented SAS images we compensate for the sensor beampattern and frequency response, before applying a tapered cosine window (Tukey window) with roundoff over a border covering 10% of the wavenumber domain area included for imaging.

In Fig. 3 we presented an example image from HISAS LF data showing a 1.2 m x 1.2 m concrete block next to a 0.9 m diameter pipeline. The bandwidth within $|K_x/(4\pi/\Delta R)| < 0.5$ was processed and is represented in the image. Some sidelobes can be observed as a result of the low sidelobe suppression of the tapered cosine window. Though the high frequency part of the scattering marked (B) is folded down into the image along-track bandwidth, any effect of folding is not easily observed.

Another example that shows the potential damaging effect of grating lobes on a wideband system is given in Fig. 15 and Fig. 16, using data from the LF band of the HISAS LF SAS prototype. The scene contains a pipeline with broadside at around 30 degrees azimuth. The collected image wavenumber data before windowing is presented in Fig. 16, and we observe that the strong scattering off the pipeline gives rise to a defocused grating lobe signal on the lower along-track wavenumbers. The upper and lower images in Fig. 15 have been formed from an along-track wavenumber interval of 0.5 normalized units width around $K_x/(4\pi/\Delta_R) = 0$ (broadside) and around $K_x/(4\pi/\Delta_R) = -0.5$ respectively. The grating lobe from the pipeline is clearly visible in the lower image, though not as a replica of the pipeline, but as a blurred feature distributed over a large area.

We also tried to illustrate the effect of grating lobes on a small reflector resembling a point scatterer and not a pipeline. This could have provided an estimate of the point spread function, and thus images from subsections of the image wavenumber domain should illustrate how the SGR change with $\boldsymbol{K}$. Due to the widebeam and wideband nature of the HISAS LF data, grating lobe smearing significantly lowers the peak level of the grating lobe contamination. So much so that we were unable to visualize grating lobe contaminations from weaker scattering targets, even those with target strength of up to 35 dB over the seafloor background.

In Fig. 17 we present an example image from MUD operated in the vertical configuration, depicting a deployed chain and a 1.5 m long epoxy-filled cylinder that are completely buried in a muddy seabed. Also here the bandwidth within $|K_x/(4\pi/\Delta R)| < 0.5$ was processed and is represented in the image. We do not present the wavenumber domain spectrum for this image, as it does not reveal any observable features. The predicted SGR was about 0 dB for this system in Fig. 13, but despite this we can still observe the chain and the cylinder

DOI til publisert versjon / DOI to published version: 10.1109/JOE.2016.2614717

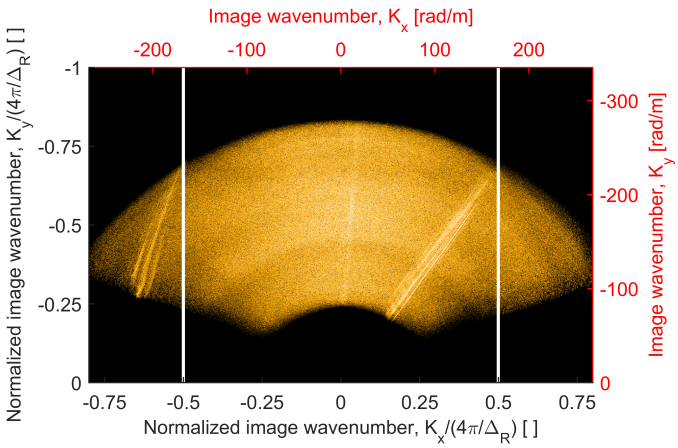

Fig. 16: The collected image wavenumber spectrum of the scene imaged in Fig. 15. The strong scattering off the pipeline around 30 degrees can be observed, along with its grating lobe replica distributed over the span from -30 to -60 degrees.

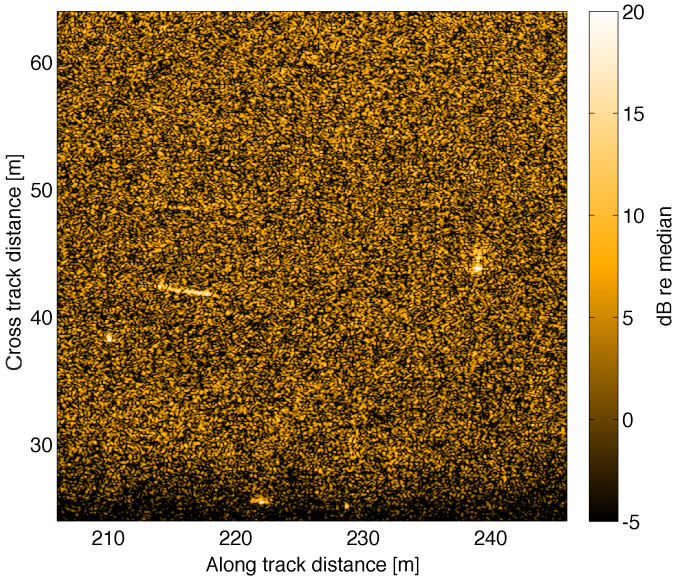

Fig. 17: Example image from MUD with sampling corresponding to Fig. 13. The image was formed using the WBP method on the interval $|K_x/(4\pi/\Delta R)| < 0.5$.

at positions $[x, y] = [218\ \mathrm{m}, 42\ \mathrm{m}]$ and $[x, y] = [238\ \mathrm{m}, 44\ \mathrm{m}]$, respectively. This supports our suggestion that we can be able to observe (persistent) targets also when zero or negative SGR is predicted for the speckle case.

C. Theoretical Results on Full-Band Image Quality

The SGR averaged over the processed wavenumber domain spectrum gives an image quality metric, or a system quality metric regarding image generation. Whilst not the main thrust of this paper, the ISIGR metric from (13) gives insight into the various SAS systems used here. We present the ISIGR as a function of processing bandwidth for each system assuming a straightforward beampattern weighting. The results are given as a function of integration limit on K_x for the under-sampled region (or any $K_y/(4\pi/\Delta_R) > 1$), in Fig. 18, and for a region covering well-sampled data broadside out to $|K_x|/(4\pi/\Delta_R) \approx 0.3$, and under-sampled data further away from the broadside direction (that is $K_y/(4\pi/\Delta_R) \approx 2/3$), in Fig. 19.

As expected, we observe that the ISIGR is lower for the purely under-sampled case than for the case also covering well-sampled data. Numerical results for a few variations on the sensor design and processing widths are available in [32, Section 5.4.1] and [34, Section 3.7.2].

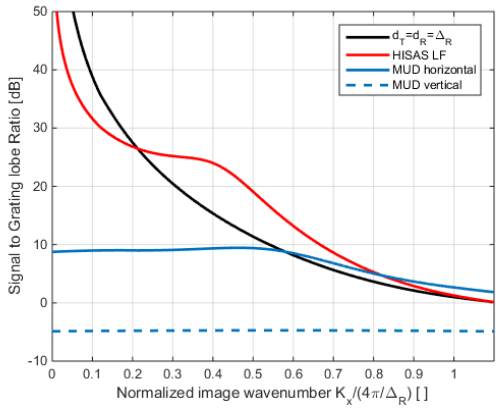

Fig. 18: Estimated spatial domain SGR on a speckle scene, using Eq. (13) evaluated in the under-sampled region as function of integration limit K_x. The different systems correspond to the sensor designs of Fig. 10 through Fig. 13, evaluated at any $K_y(4\pi/\Delta_R) > 1$. The only weighting applied is from the sensor beampattern.

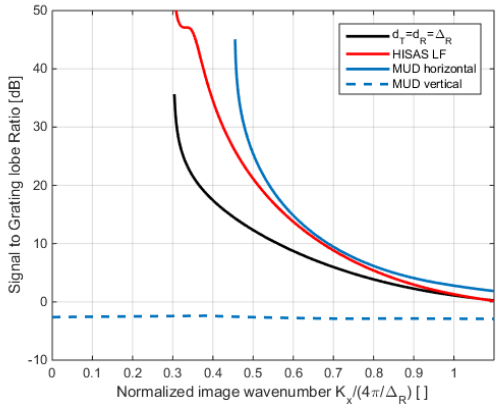

Fig. 19: Estimated spatial domain SGR on a speckle scene, using Eq. (13) evaluated at the center of the LF bands as function of integration limit K_x. For the theoretical system of $d_T = d_R = \Delta_R$, the SGR has been evaluated at $K_y/(4\pi/\Delta_R) \approx 2/3$ as for HISAS LF. For the other systems, the SGR have been evaluated at $K_y/(4\pi/\Delta_R) = \Delta_R/\lambda_{c_x}$, where λ_{c_x} is the observed wavelength at the center frequency projected onto the x-axis. The only weighting applied is from the sensor beampattern.

DOI til publisert versjon / DOI to published version: 10.1109/JOE.2016.2614717

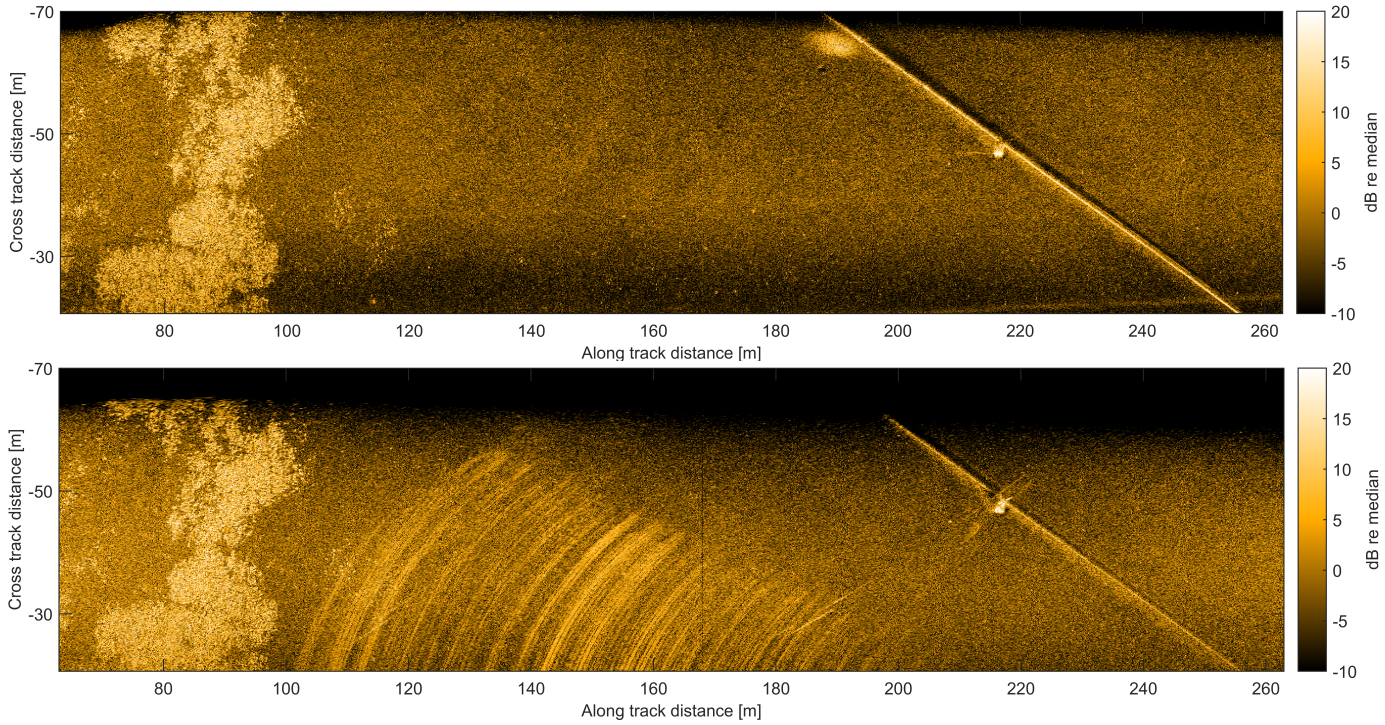

Fig. 15: SAS images from two different along-track processing bands on the same set of image wavenumber data, illustrated in Fig. 16. In the upper panel, we have processed an interval of $\Delta K_x/(4\pi/\Delta R) = 0.5$ centered on $K_x/(4\pi/\Delta R) = 0$, while in the lower panel, the same bandwidth was processed centered on $K_x/(4\pi/\Delta R) = -0.5$. The scene contains a pipeline with broadside at around 30 degrees and a concrete block, situated on a rather homogeneous seafloor with patches of Posedonia sea-grass on the left. The suboptimal lower image reveals a strong influence from grating lobes. The data were collected by HISAS with a LF prototype transmitter from the HUGIN HUS AUV during ARISE'12.

VII. Conclusion

Wideband and widebeam systems provide information on the frequency- and aspect-dependence of the scattering. A starting point for extracting this frequency- and aspect-dependence is to form a SAS image product with maximum support of high-quality data. We have suggested a new approach for evaluating the quality of the collected data, where we map the quality of the collected data over the wavenumber domain in terms of both signal to ambient noise level and signal to grating lobe level. The signal to grating lobe level is the dominating term for typical SAS designs where the along-track aperture is under-sampled for a part of the frequency band. We have provided predictions on the wavenumber domain data quality both for a typical SAS design, and for two experimental systems. We have summarized three alternative methods of synthetic aperture sonar processing based on time domain back projection, and evaluated how they access data over the wavenumber domain. We observe that the wideband back projection (WBP) algorithm provides the maximum support of information on the frequency- and aspect-dependence over the scene, though to an additional computational cost. The added information does not necessarily lead to an improved quality of the corresponding spatial domain image.

Acknowledgements

The authors would like to thank the SAS development team at Kongsberg Maritime; Terje Gunnar Fossum, Johannes Martens Anderssen and Bjørnar Langli for excellent collaboration during the integration of the LF prototype extension to HISAS. We also thank the NATO Centre for Maritime Research and Experimentation (CMRE) for facilitating the ARISE'12 scientific measurement campaign where we participated with FFI's HUGIN HUS AUV.

References

[1] R. E. Hansen, "Introduction to synthetic aperture sonar," in *Sonar Systems*, N. Z. Kolev, Ed. Intech, Sep. 2011, ch. 1, pp. 3–28, [Online]. Available: http://www.intechopen.com/books/sonar-systems.

[2] M. P. Hayes and P. T. Gough, "Synthetic aperture sonar: A review of current status," *IEEE J. Oceanic Eng.*, vol. 34, no. 3, pp. 207–224, Jul. 2009.

[3] S. G. Schock, A. Tellier, J. Wulf, J. Sara, and M. Ericksen, "Buried object scanning sonar," *IEEE J. Ocean. Eng.*, vol. 26, no. 4, pp. 677–689, Oct. 2001.

[4] J. T. Christoff, J. E. Fernandez, and D. A. Cook, "Unmanned underwater vehicle broadband synthetic aperture sonar," in *Proc. OCEANS'02 MTS/IEEE Conf.*, Biloxi, Mississippi, Oct. 2002, pp. 1871–1877.

[5] K. L. Williams, S. G. Kargl, E. I. Thorsos, D. S. Burnett, J. L. Lopes, M. Zampolli, and P. L. Marston, "Acoustic scattering from a solid aluminum cylinder in contact with a sand sediment: measurements, modeling, and interpretation." *J. Acoust. Soc. Am.*, vol. 127, no. 6, pp. 3356–71, Jun. 2010.

[6] S. A. V. Synnes and R. E. Hansen, "Aspect-dependent scattering in widebeam synthetic aperture sonar," in *Proc. 3rd Underwater Acoustics Conference and Exhibition (UACE2015)*, Creete, Greece, 2015, p. 8.

DOI til publisert versjon / DOI to published version: 10.1109/JOE.2016.2614717

[7] A. J. Hunter and R. v. Vossen, "Sonar target enhancement by schrinkage of incoherent wavelet coefficients," *J. Acoust. Soc. Am.*, vol. 135, no. 1, pp. 262–268, Jan. 2014.
[8] P. L. Nielsen, R. D. Hollett, G. Canepa, and W. L. J. Fox, "Unique low-frequency mine hunting and seabed characterization sonar," in *Proc. 1st Int. Conf. and Exhib. on Underwater Acoustics (UA 2013)*, Corfu, Greece, Jun. 2013, pp. 385–392.
[9] D. D. Sternlicht, J. E. Fernandez, and T. M. Dr. Marston, "Advances in synthetic aperture sonar transform mine countermeasures and undersea warfare," *CHIPS Magazine*, Apr.-Jun. 2013, [Online]. Available: http://www.doncio.navy.mil/CHIPS.
[10] Ø. Ødegård, M. Ludvigsen, and P. A. Lågstad, "Using synthetic aperture sonar in marine archaeological surveys - some first experiences," in *Proc. OCEANS'13 MTS/IEEE Conf.*, Bergen, Norway, Jun. 2013.
[11] J. Châtillon, A. E. Adams, M. A. Lawlor, and M. E. Zakharia, "Sami: A low-frequency prototype for mapping and imaging of the seabed by means of synthetic aperture," *IEEE J. Ocean. Eng.*, vol. 24, no. 1, pp. 4–15, Jan. 1999.
[12] G. Beckers, R. v. Vossen, and G. Vlaming, "Low-frequency synthetic aperture sonar for detecting explosives in harbors," *Sea Technology Magazine*, pp. 15–17, Mar. 2012.
[13] S. A. V. Synnes and R. E. Hansen, "Ultra wideband sas imaging," in *Proc. 1st Int. Conf. and Exhib. on Underwater Acoustics (UA 2013)*, Corfu, Greece, Jun. 2013, pp. 111–118.
[14] D. H. Johnson and D. E. Dudgeon, *Array Signal Processing: Concepts and Techniques*. Upper Saddle River, NJ, USA: Prentice Hall, 1993.
[15] M. Soumekh, *Synthetic Aperture Radar Signal Processing*. New York, NY, USA: John Wiley & Sons, 1999.
[16] I. G. Cumming and F. H. Wong, *Digital Processing of Synthetic Aperture Radar Data: Algorithms and Implementation*. Norwood, MA, USA: Artech House, 2005.
[17] G. Franceschetti and R. Lanari, *Synthetic Aperture Radar Processing*. New York, USA: CRC Press, 1999.
[18] B. G. Ferguson and R. J. Wyber, "Generalized framework for real aperture, synthetic aperture, and tomographic sonar imaging," *IEEE J. Ocean. Eng.*, vol. 34, no. 3, pp. 225–238, Jul. 2009.
[19] S. Madsen, "Motion compensation for ultra wide band sar," in *IEEE Geoscience and Remote Sensing Symposium. IGARSS'01*, vol. 3, July 2001, pp. 1436–1438.
[20] O. Frey, C. Magnard, M. Rüegg, and E. Meier, "Focusing of airborne synthetic aperture radar data from highly nonlinear flight tracks," *IEEE Trans. Geosci. Remote Sens.*, vol. 47, no. 6, pp. 1844–1858, Jun. 2009.
[21] J. Châtillon, M.-E. Bouhier, and M. Zakharia, "Synthetic aperture sonar for seabed imaging: relative merits of narrow-band and wide-band approaches," *IEEE J. Ocean. Eng.*, vol. 17, no. 1, pp. 95–105, Jan. 1992.
[22] M. P. Hayes and P. T. Gough, "Broad-band synthetic aperture sonar," *IEEE J. Ocean. Eng.*, vol. 17, no. 1, pp. 80–94, Jan. 1992.
[23] W. G. Carrara, R. S. Goodman, and R. M. Majewski, *Spotlight Synthetic Aperture Radar: Signal Processing Algorithms*. Norwood, MA, USA: Artech House, 1995.
[24] J. C. Curlander and R. N. McDonough, *Synthetic Aperture Radar System and Signal Processing*. New York, USA: John Wiley & Sons, Inc, 1991.
[25] R. E. Hansen, H. J. Callow, T. O. Sæbø, and S. A. V. Synnes, "Challenges in seafloor imaging and mapping with synthetic aperture sonar," *IEEE Trans. Geosci. Remote Sens.*, vol. 49, no. 10, pp. 3677–3687, Oct. 2011.
[26] M. Soumekh, *Fourier Array Imaging*. Englewood Cliffs, NJ, USA: Prentice Hall, 1994.
[27] A. Ishimaru, *Wave Propagation and Scattering in Random Media*. New York, NY, USA: Academic Press, 1978.
[28] A. W. Rihaczek and S. J. Hershkowitz, "Man-made target backscattering behavior: Applicability of conventional radar resolution theory," *IEEE Trans. Aerosp. and Electron. Syst.*, vol. 32, no. 2, pp. 809–824, 1996.
[29] G. M. Wenz, "Acoustic ambient noise in the ocean: Spectra and sources," *J. Acoust. Soc. Am.*, vol. 34, no. 12, pp. 1936–56, Dec. 1962.
[30] K. D. Rolt and H. Schmidt, "Azimuthal ambiguities in synthetic aperture sonar and synthetic aperture radar imagery," *IEEE J. Ocean. Eng.*, vol. 17, no. 1, pp. 73–79, Jan. 1992.
[31] A. Moreira, "Suppressing the azimuth ambiguities in synthetic aperture radar images," *IEEE Trans. Geosci. Remote Sens.*, vol. 31, no. 4, pp. 885–895, Jul. 1993.
[32] D. W. Hawkins, "Synthetic aperture imaging algorithms: with application to wide bandwidth sonar," Ph.D. thesis, University of Canterbury, Christchurch, New Zealand, Oct. 1996.
[33] A. Hunter, R. van Vossen, B. Quesson, and G. Beckers, "Acoustic signatures of underwater uxo measured by low frequency broadband sas," in *Proc. 1st Int. Conf. and Exhib. on Underwater Acoustics (UA 2013)*, Corfu, Greece, Jun. 2013, pp. 865–872.
[34] P. J. Barclay, "Interferometric synthetic aperture sonar design and performance," Ph.D. thesis, University of Canterbury, Christchurch, New Zealand, Aug. 2007.

Stig Asle Vaksvik Synnes (M'13) was born in Ålesund, Norway, in 1972. He received his M.Sc. degree in atomic physics from the University of Bergen, Norway, in 1997. Since 1998, he has been with the Norwegian Defence Research Establishment (FFI), Kjeller, Norway. His main research interests are on electromagnetic sensors, naval mine countermeasures and synthetic aperture sonar (SAS). His SAS research include shallow water sonar performance and correlation based navigation. Currently he is working on a Ph.D. in the field of wideband SAS.

Alan Joseph Hunter (M'06) was born in Christchurch, New Zealand, in 1978. He received the B.E. (Hons) and Ph.D. degrees in electrical and electronic engineering from the University of Canterbury, New Zealand, in 2001 and 2006, respectively. From 2007 to 2010, he was a research associate at the University of Bristol, England. From 2010 to 2014 he was a defence scientist at TNO, the Netherlands. Since 2014, Dr. Hunter has been a lecturer in engineering at the University of Bath, England. Dr. Hunter's research interests are in underwater acoustics, sonar imaging of the seafloor, and autonomous underwater systems.

Roy Edgar Hansen (M'07) received the M.Sc. degree in physics in 1992, and the Ph.D. degree in physics in 1999, both from the University of Tromsø, Norway. The PhD thesis is named Measurements in the Mixed Layer by a Bistatic Multi-CW Doppler Sonar. From 1992 to 2000 he was with the Norwegian research company TRIAD, working on multistatic sonar, multistatic radar, SAR and underwater communications. Since 2000, he has been working at the Norwegian Defence Research Establishment (FFI), Kjeller, Norway, in the field of synthetic aperture sonar. He is currently principal scientist at FFI. He is also adjunct associated professor at Department of informatics at University in Oslo, Norway.

Torstein Olsmo Sæbø (M'06 - SM'13) was born in Bergen, Norway, in 1977. He received the cand.scient (M.Sc.) degree in astrophysics from the University of Oslo, Oslo, Norway, in 2002 and the Ph.D. degree in physics from the University of Tromsø, Tromsø, Norway, in 2010, with a dissertation entitled Seafloor depth estimation by means of interferometric synthetic aperture sonar. Since 2002, he has been with the Norwegian Defence Research Establishment (FFI), Kjeller, Norway, specializing in the field of interferometry on synthetic aperture sonar. Dr. Sb is currently research manager for the marine robotics development and the synthetic aperture sonar development at FFI. He is also Associate Editor for the IEEE JOURNAL OF OCEANIC ENGINEERING.

DOI til publisert versjon / DOI to published version: 10.1109/JOE.2016.2614717

Hayden John Callow (M'07) was born in Invercargill, New Zealand, in 1978. He received a B.E. (Hons I) and Ph.D. in Electrical and Electronic Engineering from the University of Canterbury in 1999 and 2003 respectively. After completing his PhD work in SAS imaging and autofocus he joined at the Norwegian Defence Research Establishment (FFI) in 2004 where he worked within the AUV research team on SAS imaging sensors; primarily performing research into SAS design, beamforming, micronavigation and interferometry. In 2011 he joined Kongsberg Maritime where he works as a SAS R&D Engineer.

Robbert van Vossen was born in Raamsdonk, the Netherlands, in 1977. He received his M.Sc. degree in Geophysics from Utrecht University in 2000 and in 2005 his Ph.D. in Seismology (cum laude), which was conducted in collaboration with Schlumberger Cambridge Research. He is currently Senior Research Scientist in the Acoustics and Sonar Department of The Netherlands Organisation for Applied Scientific Research (TNO). His research interests are signal processing, image interpretation, autonomy, and performance modeling for anti-submarine warfare and naval mine-counter measures applications.

Andreas Austeng (M'97) was born in Oslo, Norway, in 1970. He received the M.Sc. degree in physics in 1996 and the Ph.D. degree in computer science in 2001, both from the University of Oslo. Since 2001, he has been working at the Department of Informatics, University of Oslo, first as a postdoctoral research fellow, and currently as an Associate Professor. His research interests include signal processing for acoustical imaging.

DOI til publisert versjon / DOI to published version: 10.1109/JOE.2016.2614717